

## Updated High-Temperature Opacities for The Dartmouth Stellar Evolution Program and their Effect on the Jao Gap Location

2 THOMAS M. BOUDREAUX<sup>1</sup> AND BRIAN C. CHABOYER<sup>1</sup>

3 *<sup>1</sup>Department of Physics and Astronomy, Dartmouth College, Hanover, NH 03755, USA*

### 4 ABSTRACT

5 The Jao Gap, a 17 percent decrease in stellar density at  $M_G \sim 10$  identified in both Gaia DR2  
6 and EDR3 data, presents a new method to probe the interior structure of stars near the fully con-  
7 vective transition mass. The Gap is believed to originate from convective kissing instability wherein  
8 asymmetric production of  $^3\text{He}$  causes the core convective zone of a star to periodically expand and  
9 contract and consequently the stars' luminosity to vary. Modeling of the Gap has revealed a sensitivity  
10 in its magnitude to a population's metallicity primarily through opacity. Thus far, models of the Jao  
11 Gap have relied on OPAL high-temperature radiative opacities. Here we present updated synthetic  
12 population models tracing the Gap location modeled with the Dartmouth stellar evolution code using  
13 the OPLIB high-temperature radiative opacities. Use of these updated opacities changes the predicted  
14 location of the Jao Gap by  $\sim 0.05$  mag as compared to models which use the OPAL opacities. This  
15 difference is likely too small to be detectable in empirical data.

16 *Keywords:* Stellar Evolution (1599) — Stellar Evolutionary Models (2046)

### 17 1. INTRODUCTION

18 Due to the initial mass requirements of the molecular  
19 clouds which collapse to form stars, star formation is  
20 strongly biased towards lower mass, later spectral class  
21 stars when compared to higher mass stars. Partly as  
22 a result of this bias and partly as a result of their ex-  
23 tremely long main-sequence lifetimes, M Dwarfs make  
24 up approximately 70 percent of all stars in the galaxy.  
25 Moreover, some planet search campaigns have focused  
26 on M Dwarfs due to the relative ease of detecting small  
27 planets in their habitable zones (e.g. Nutzman & Char-  
28 bonneau 2008). M Dwarfs then represent both a key  
29 component of the galactic stellar population as well as  
30 the possible set of stars which may host habitable ex-  
31 oplanets. Given this key location M Dwarfs occupy in  
32 modern astronomy it is important to have a thorough  
33 understanding of their structure and evolution.

34 Jao et al. (2018) discovered a novel feature in the Gaia  
35 Data Release 2 (DR2)  $G_{BP} - G_{RP}$  color-magnitude-  
36 diagram. Around  $M_G = 10$  there is an approximately

37 17 percent decrease in stellar density of the sample of  
38 stars Jao et al. (2018) considered. Subsequently, this  
39 has become known as either the Jao Gap, or Gaia M  
40 Dwarf Gap. Following the initial detection of the Gap  
41 in DR2 the Gap has also potentially been observed in  
42 2MASS (Skrutskie et al. 2006; Jao et al. 2018); however,  
43 the significance of this detection is quite weak and it re-  
44 lies on the prior of the Gap's location from Gaia data.  
45 Further, the Gap is also present in Gaia Early Data Re-  
46 lease 3 (EDR3) (Jao & Feiden 2021). These EDR3 and  
47 2MASS data sets then indicate that this feature is not  
48 a bias inherent to DR2.

49 The Gap is generally attributed to convective instabil-  
50 ities in the cores of stars straddling the fully convective  
51 transition mass (0.3 - 0.35  $M_\odot$ ) (Baraffe & Chabrier  
52 2018). These instabilities interrupt the normal, slow,  
53 main sequence luminosity evolution of a star and result  
54 in luminosities lower than expected from the main se-  
55 quence mass-luminosity relation (Jao & Feiden 2020).

56 The Jao Gap, inherently a feature of M Dwarf pop-  
57 ulations, provides an enticing and unique view into the  
58 interior physics of these stars (Feiden et al. 2021). This  
59 is especially important as, unlike more massive stars,  
60 M Dwarf seismology is infeasible due to the short peri-  
61 ods and extremely small magnitudes which both radial  
62 and low-order low-degree non-radial seismic waves are

Corresponding author: Thomas M. Boudreax  
thomas.m.boudreaux.gr@dartmouth.edu,  
thomas@boudreauxmail.com

<sup>63</sup> predicted to have in such low mass stars (Rodríguez-  
<sup>64</sup> López 2019). The Jao Gap therefore provides one of the  
<sup>65</sup> only current methods to probe the interior physics of M  
<sup>66</sup> Dwarfs.

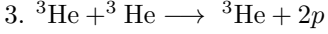
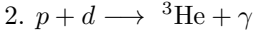
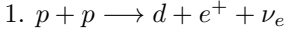
<sup>67</sup> Despite the early success of modeling the Gap some  
<sup>68</sup> issues remain. Jao & Feiden (2020, 2021) identify that  
<sup>69</sup> the Gap has a wedge shape which has not been successful  
<sup>70</sup> reproduced by any current modeling efforts and which  
<sup>71</sup> implies a somewhat unusual population composition of  
<sup>72</sup> young, metal-poor stars. Further, Jao & Feiden (2020)  
<sup>73</sup> identify substructure, an additional over density of stars,  
<sup>74</sup> directly below the Gap, again a feature not yet fully  
<sup>75</sup> captured by current models.

<sup>76</sup> All currently published models of the Jao Gap make  
<sup>77</sup> use of OPAL high temperature radiative opacities. Here  
<sup>78</sup> we investigate the effect of using the more up-to-  
<sup>79</sup> date OPLIB high temperature radiative opacities and  
<sup>80</sup> whether these opacity tables bring models more in line  
<sup>81</sup> with observations. In Section 2 we provide an overview  
<sup>82</sup> of the physics believed to result in the Jao Gap, in  
<sup>83</sup> Section 3 we review the differences between OPAL  
<sup>84</sup> and OPLIB and describe how we update DSEP to use  
<sup>85</sup> OPLIB opacity tables. Section 4 walks through the stel-  
<sup>86</sup> lar evolution and population synthesis modeling we per-  
<sup>87</sup> form. Finally, in Section 5 we present our findings.

## 2. JAO GAP

<sup>88</sup> A theoretical explanation for the Jao Gap (Figure 1)  
<sup>89</sup> comes from van Saders & Pinsonneault (2012) and Mac-  
<sup>90</sup> Donald & Gizis (2018), who propose that in a star di-  
<sup>91</sup> rectly above the transition mass, due to asymmetric pro-  
<sup>92</sup> duction and destruction of  $^3\text{He}$  during the proton-proton  
<sup>93</sup> I chain (ppI), periodic luminosity variations can be in-  
<sup>94</sup> duced. This process is known as convective-kissing in-  
<sup>95</sup> stability. Very shortly after the zero-age main sequence  
<sup>96</sup> such a star will briefly develop a radiative core; however,  
<sup>97</sup> as the core temperature exceeds  $7 \times 10^6$  K, enough en-  
<sup>98</sup> ergy will be produced by the ppI chain that the core once  
<sup>99</sup> again becomes convective. At this point the star exists  
<sup>100</sup> with both a convective core and envelope, in addition  
<sup>101</sup> to a thin, radiative layer separating the two. Subse-  
<sup>102</sup> quently, asymmetries in ppI affect the evolution of the  
<sup>103</sup> star's convective core.

<sup>104</sup> The proton-proton I chain constitutes three reactions



<sup>105</sup> Initially, reaction 3 of ppI consumes  $^3\text{He}$  at a slower  
<sup>106</sup> rate than it is produced by reaction 2 and as a result,  
<sup>107</sup> the core  $^3\text{He}$  abundance and consequently the rate of

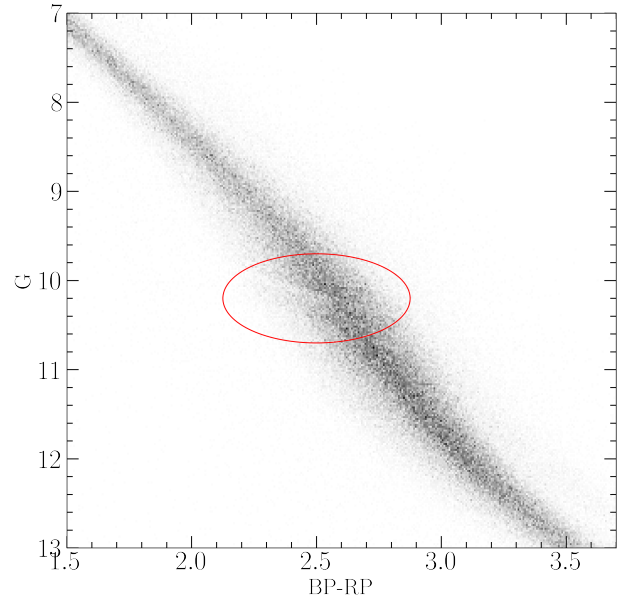


**Figure 1.** The Jao Gap (circled) seen in the Gaia Catalogue of Nearby Stars (Gaia Collaboration et al. 2021).

<sup>112</sup> reaction 3, increases with time. The core convective  
<sup>113</sup> zone expands as more of the star becomes unstable to  
<sup>114</sup> convection. This expansion continues until the core con-  
<sup>115</sup> nects with the convective envelope. At this point convec-  
<sup>116</sup> tive mixing can transport material throughout the entire  
<sup>117</sup> star and the high concentration of  $^3\text{He}$  rapidly diffuses  
<sup>118</sup> outward, away from the core, decreasing energy genera-  
<sup>119</sup> tion as reaction 3 slows down. Ultimately, this leads to  
<sup>120</sup> the convective region around the core pulling back away  
<sup>121</sup> from the convective envelope, leaving in place the radi-  
<sup>122</sup> ative transition zone, at which point  $^3\text{He}$  concentrations  
<sup>123</sup> grow in the core until it once again expands to meet  
<sup>124</sup> the envelope. These periodic mixing events will con-  
<sup>125</sup> tinue until  $^3\text{He}$  concentrations throughout the star reach  
<sup>126</sup> an equilibrium ultimately resulting in a fully convective  
<sup>127</sup> star. Figure 2 traces the evolution of a characteristic  
<sup>128</sup> star within the Jao Gap's mass range.

### 2.1. Efforts to Model the Gap

<sup>129</sup> Since the identification of the Gap, stellar modeling  
<sup>130</sup> has been conducted to better constrain its location, ef-  
<sup>131</sup> fects, and exact cause. Both Mansfield & Kroupa (2021)  
<sup>132</sup> and Feiden et al. (2021) identify that the Gap's mass lo-  
<sup>133</sup>cation is correlated with model metallicity — the mass-  
<sup>134</sup> luminosity discontinuity in lower metallicity models be-  
<sup>135</sup> ing at a commensurately lower mass. Feiden et al. (2021)  
<sup>136</sup> suggests this dependence is due to the steep relation of  
<sup>137</sup> the radiative temperature gradient,  $\nabla_{rad}$ , on tempera-  
<sup>138</sup> ture and, in turn, on stellar mass.

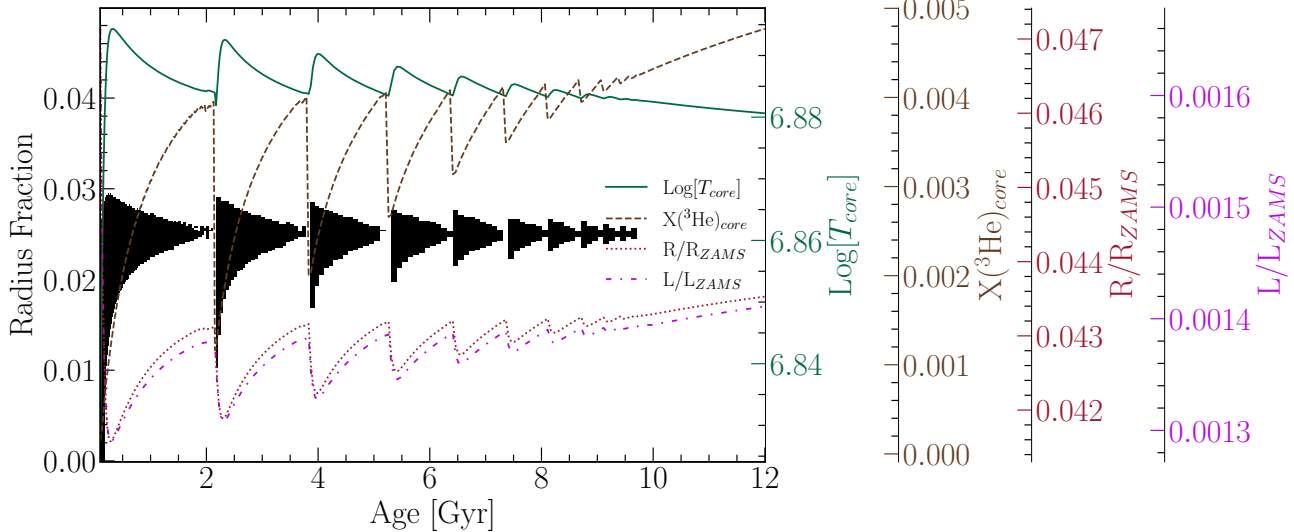


**Figure 2.** Diagram for a characteristic stellar model of  $0.35625 M_{\odot}$  which is within the Jao Gap’s mass range. The black shaded regions denote whether, at a particular model age, a radial shell within the model is radiative (with white meaning convective). The lines trace the models core temperature, core  ${}^3\text{He}$  mass fraction, fractional luminosity wrt. the zero age main sequence and fractional radius wrt. the zero age main sequence.

$$\nabla_{rad} \propto \frac{L\kappa}{T^4} \quad (1)$$

As metallicity decreases so does opacity, which, by Equation 1, dramatically lowers the temperature at which radiation will dominate energy transport (Chabrier & Baraffe 1997). Since main sequence stars are virialized the core temperature is proportional to the core density and total mass. Therefore, if the core temperature where convective-kissing instability is expected decreases with metallicity, so too will the mass of stars which experience such instabilities.

The strong opacity dependence of the Jao Gap begs the question: **what is the effect of different opacity calculations on Gap properties.** As we can see above, changing opacity should affect the Gap’s location in the mass-luminosity relation and therefore in a color-magnitude diagram. Moreover, current models of the Gap have yet to locate it precisely in the CMD (Feiden et al. 2021) with an approximate 0.16 G-magnitude difference between the observed and modeled Gaps. Opacity provides one, as yet unexplored, parameter which has the potential to resolve these discrepancies.

### 3. UPDATED OPACITIES

Multiple groups have released high-temperature opacities including, the Opacity Project (OP Seaton et al. 1994), Laurence Livermore National Labs OPAL opacity tables (Iglesias & Rogers 1996), and Los Alamos National Labs OPLIB opacity tables (Colgan et al. 2016). OPAL high-temperature radiative opacity tables

in particular are very widely used by current generation isochrone grids (e.g. Dartmouth, MIST, & StarEvol, Dotter et al. 2008; Choi et al. 2016; Amard et al. 2019). OPLIB opacity tables (Colgan et al. 2016) are not widely used but include the most up-to-date plasma modeling. While the overall effect on the CMD of using OPLIB compared to OPAL tables is small, the strong theoretical opacity dependence of the Jao Gap raises the potential for these small effects to measurably shift the Gap’s location. We update DSEP to use high temperature opacity tables based on measurements from Los Alamos national Labs T-1 group (OPLIB, Colgan et al. 2016). The OPLIB tables are created with ATOMIC (Magee et al. 2004; Hakel et al. 2006; Fontes et al. 2015), a modern LTE and non-LTE opacity and plasma modeling code. These updated tables were initially created in an attempt to resolve the discrepancy between helioseismic and solar model predictions of chemical abundances in the sun (Bahcall et al. 2005).

OPLIB tables include monochromatic Rosseland mean opacities — composed from bound-bound, bound-free, free-free, and scattering opacities — for elements hydrogen through zinc over temperatures  $0.5\text{eV}$  to  $100\text{ keV}$  ( $5802\text{ K}$  –  $1.16 \times 10^9\text{ K}$ ) and for mass densities from approximately  $10^{-8}\text{ g cm}^{-3}$  up to approximately  $10^4\text{ g cm}^{-3}$  (though the exact mass density range varies as a function of temperature).

DSEP ramps the Ferguson et al. (2005) low temperature opacities to high temperature opacities tables between  $10^{4.3}\text{ K}$  and  $10^{4.5}\text{ K}$ ; therefore, only differences between high-temperature opacity sources above  $10^{4.3}$

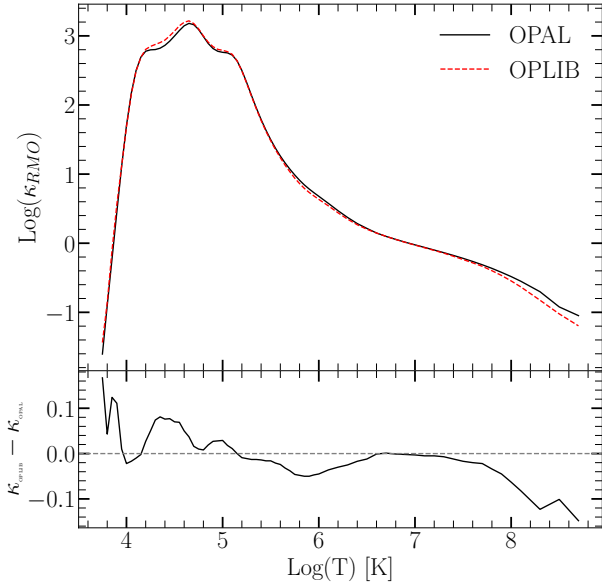


**Figure 3.** Rosseland mean opacity with the GS98 solar composition for both OPAL opacities and OPLIB opacities (top). Residuals between OPLIB opacities and OPAL opacities (bottom). These opacities are plotted at  $\log_{10}(R) = -1.5$ ,  $X = 0.7$ , and  $Z = 0.02$ . Note how the OPLIB opacities are systematically lower than the OPAL opacities for temperatures above  $10^5$  K.

K can effect model evolution. When comparing OPAL and OPLIB opacity tables (Figure 3) we find OPLIB opacities are systematically lower than OPAL opacities for temperatures above  $10^5$  K. Between  $10^{4.3}$  and  $10^5$  K OPLIB opacities are larger than OPAL opacities. These generally lower opacities will decrease the radiative temperature gradient throughout much of the radius of a model.

### 3.1. Table Querying and Conversion

The high-temperature opacity tables used by DSEP and most other stellar evolution programs give Rosseland-mean opacity,  $\kappa_R$ , along three dimensions: temperature, a density proxy  $R$  (Equation 2;  $T_6 = T \times 10^{-6}$ ,  $\rho$  is the mass density), and composition.

$$R = \frac{\rho}{T_6^3} \quad (2)$$

OPLIB tables may be queried from a web interface<sup>1</sup>; however, OPLIB opacities are parametrized using mass density and temperature instead of  $R$  and temperature. It is most efficient for us to convert these tables to the OPAL format instead of modifying DSEP

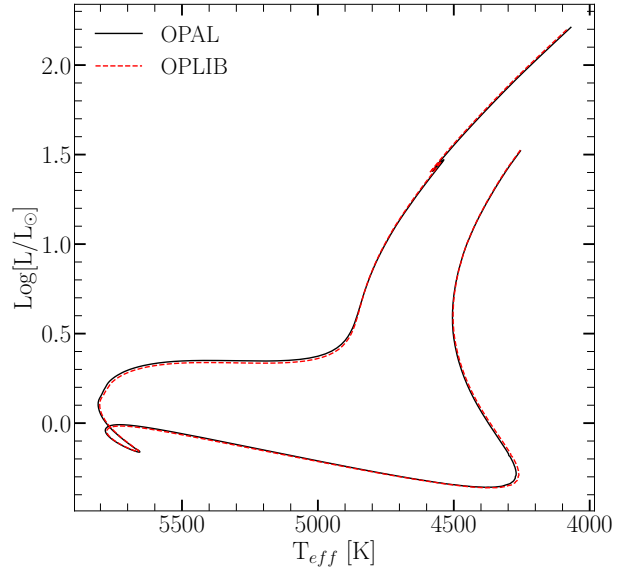


**Figure 4.** HR Diagram for the two SCSMs, OPAL and OPLIB. OPLIB is shown as a red dashed line.

to use the OPLIB format directly. In order to generate many tables easily and quickly we develop a web scraper (`pyTOPSScrape`, Boudreault 2022) which can automatically retrieve all the tables needed to build an opacity table in the OPAL format. `pyTOPSScrape`<sup>2</sup> has been released under the permissive MIT license with the consent of the Los Alamos T-1 group. For a detailed discussion of how the web scraper works and how OPLIB tables are transformed into a format DSEP can use see Appendices A & B.

### 3.2. Solar Calibrated Stellar Models

In order to validate the OPLIB opacities, we generated a solar calibrated stellar model (SCSM) using these new tables. We first manually calibrate the surface  $Z/X$  abundance to within one part in 100 of the solar value. Subsequently, we allow both the convective mixing length parameter,  $\alpha_{ML}$ , and the initial Hydrogen mass fraction,  $X$ , to vary simultaneously, minimizing the difference, to within one part in  $10^5$ , between resultant models' final radius and luminosity to those of the sun. Finally, we confirm that the model's surface  $Z/X$  abundance is still within one part in 100 of the solar value.

Solar calibrated stellar models evolved using GS98 OPAL and OPLIB opacity tables (Figure 4) differ  $\sim 0.5\%$  in the SCSM hydrogen mass fractions and  $\sim 1.5\%$  in the SCSM convective mixing length parameters (Table 1). While the two evolutionary tracks are very sim-

<sup>1</sup> <https://aphysics2.lanl.gov/apps/>

<sup>2</sup> <https://github.com/tboudreault/pytopsscrape>

| Model | $X$    | $\alpha_{ML}$ |
|-------|--------|---------------|
| OPAL  | 0.7066 | 1.9333        |
| OPLIB | 0.7107 | 1.9629        |

**Table 1.** Optimized parameters for SCSMs evolved using OPAL and OPLIB high temperature opacity tables.

ilar, note that the OPLIB SCSM's luminosity is systematically lower past the solar age. While at the solar age the OPLIB SCSM luminosity is effectively the same as the OPAL SCSM. This luminosity difference between OPAL and OPLIB based models is not inconsistent with expectations given the more shallow radiative temperature gradient resulting from the lower OPLIB opacities

#### 4. MODELING

In order to model the Jao Gap we evolve two extremely finely sampled mass grids of models. One of these grids uses the OPAL high-temperature opacity tables while the other uses the OPLIB tables (Figure 5). Each grid evolves a model every  $0.00025 M_{\odot}$  from 0.2 to  $0.4 M_{\odot}$  and every  $0.005 M_{\odot}$  from 0.4 to  $0.8 M_{\odot}$ . All models in both grids use a GS98 solar composition, the (1, 101, 0) FreeEOS (version 2.7) configuration, and 1000 year old pre-main sequence polytropic models, with polytropic index 1.5, as their initial conditions.

Because in this work we are just interested in the location shift of the Gap as the opacity source varies, we do not model variations in composition. Mansfield & Kroupa (2021); Jao & Feiden (2020); Feiden et al. (2021) all look at the effect composition has on Jao Gap location. They find that as population metallicity increases so too does the mass range and consequently the magnitude of the Gap. From an extremely low metallicity population ( $Z=0.001$ ) to a population with a more solar like metallicity this shift in mass range can be up to  $0.05 M_{\odot}$  (Mansfield & Kroupa 2021).

##### 4.1. Population Synthesis

In order to compare the Gap to observations we use in house population synthesis code. We empirically calibrate the relation between G, BP, and RP magnitudes and their uncertainties along with the parallax/G magnitude uncertainty relation using the Gaia Catalogue of Nearby Stars (GCNS, Gaia Collaboration et al. 2021) and Equations 3 & 4.  $M_g$  is the Gaia G magnitude while  $M_i$  is the magnitude in the  $i^{\text{th}}$  band, G, BP, or RP. The coefficients  $a$ ,  $b$ , and  $c$  determined using a non-linear least squares fitting routine. Equation 3 then models the relation between G magnitude and parallax uncertainty while Equation 4 models the relation between each magnitude and its uncertainty.

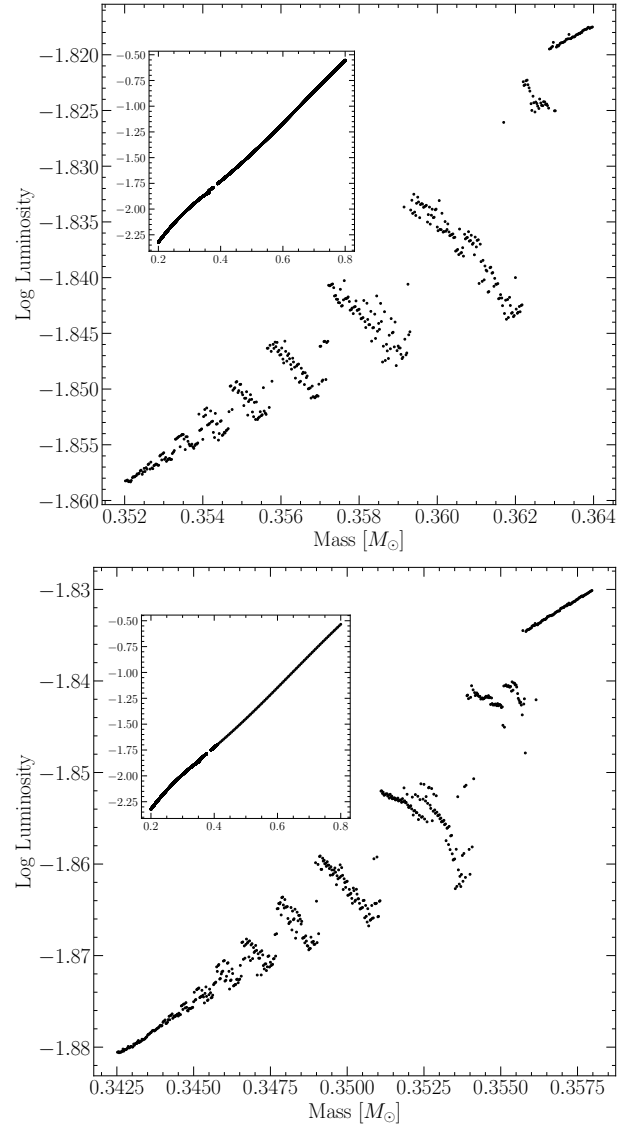


**Figure 5.** Mass-luminosity relation at 7 Gyrs for models evolved using OPAL opacity tables (top) and those evolved using OPLIB opacity tables (bottom). Note the lower mass range of the OPLIB Gap.

$$\sigma_{plx}(M_g) = ae^{bM_g} + c \quad (3)$$

$$\sigma_i(M_i) = ae^{M_i - b} + c \quad (4)$$

The full series of steps in our population synthesis code are:

1. Sample from a Sollima (2019) ( $0.25M_{\odot} < M < 1M_{\odot}$ ,  $\alpha = -1.34 \pm 0.07$ ) IMF to determine synthetic star mass.
2. Find the closest model above and below the synthetic star, linearly interpolate these models'  $T_{eff}$ ,

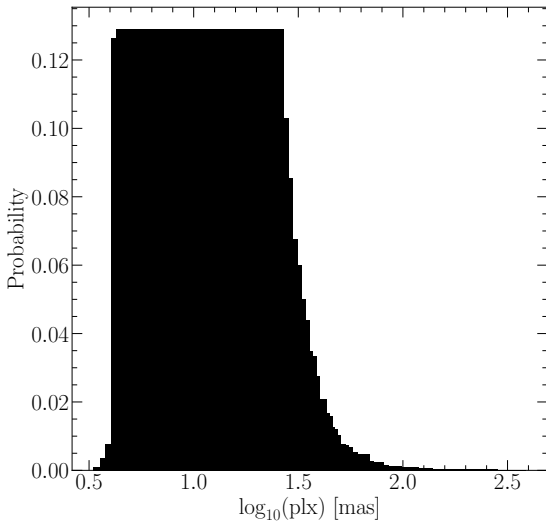


**Figure 6.** Probability distribution sampled when assigning true parallaxes to synthetic stars. This distribution is built from the GCNS and includes all stars with BP-RP colors between 2.3 and 2.9, the same color range of the Jao Gap.

304       $\log(g)$ , and  $\log(L)$  to those at the synthetic star  
305      mass.

- 306      3. Convert synthetic star  $g$ ,  $T_{eff}$ , and  $\log(L)$  to Gaia  
307      G, BP, and RP magnitudes using the Gaia (E)DR3  
308      bolometric corrections (Creevey et al. 2022) along  
309      with code obtained thorough personal communica-  
310      tion with Aaron Dotter (Choi et al. 2016).
- 311      4. Sample from the GCNS parallax distribution (Fig-  
312      ure 6), limited to stars within the BP-RP color  
313      range of 2.3 – 2.9, to assign synthetic star a “true”  
314      parallax.
- 315      5. Use the true parallax to find an apparent magni-  
316      tude for each filter.
- 317      6. Evaluate the empirical calibration given in Equa-  
318      tion 3 to find an associated parallax uncertainty.  
319      Then sample from a normal distribution with a  
320      standard deviation equal to that uncertainty to  
321      adjust the true parallax resulting in an “observed”  
322      parallax.
- 323      7. Use the “observed” parallax and the apparent  
324      magnitude to find an “observed” magnitude.
- 325      8. Fit the empirical calibration given in Equation 4  
326      to the GCNS and evaluate it to give a magnitude  
327      uncertainty scale in each band.

| Model   | Location | Prominence | Width |
|---------|----------|------------|-------|
| OPAL 1  | 10.138   | 0.593      | 0.027 |
| OPAL 2  | 10.183   | 0.529      | 0.023 |
| OPLIB 1 | 10.188   | 0.724      | 0.032 |
| OPLIB 2 | 10.233   | 0.386      | 0.027 |

**Table 2.** Locations identified as potential Gaps.

328      9. Adjust each magnitude by an amount sampled  
329      from a normal distribution with a standard devi-  
330      ation of the magnitude uncertainty scale found  
331      in the previous step.

332      This method then incorporates both photometric and  
333      astrometric uncertainties into our population synthe-  
334      sis. An example 7 Gyr old synthetic populations using  
335      OPAL and OPLIB opacities are presented in Figure 7.

336

## 5. RESULTS

337      We quantify the Jao Gap location along the magni-  
338      tude (Table 2) axis by sub-sampling our synthetic pop-  
339      ulations, finding the linear number density along the  
340      magnitude axis of each sub-sample, averaging these lin-  
341      ear number densities, and extracting any peaks above  
342      a prominence threshold of 0.1 as potential magnitudes  
343      of the Jao Gap (Figure 8). Gap widths are measured  
344      at 50% the height of the peak prominence. We use the  
345      python package `scipy` (Virtanen et al. 2020) to both  
346      identify peaks and measure their widths.

347      In both OPAL and OPLIB synthetic populations our  
348      Gap identification method finds two gaps above the  
349      prominence threshold. The identification of more than  
350      one gap is not inconsistent with the mass-luminosity  
351      relation seen in the grids we evolve. As noise is in-  
352      jected into a synthetic population smaller features will  
353      be smeared out while larger ones will tend to persist.  
354      The mass-luminosity relations shown in in Figure 5 make  
355      it clear that there are: (1), multiple gaps due to stars of  
356      different masses undergoing convective mixing events at  
357      different ages, and (2), the gaps decrease in width mov-  
358      ing to lower masses / redder. Therefore, the multiple  
359      gaps we identify are attributable to the two bluest gaps  
360      being wide enough to not smear out with noise. In fact,  
361      if we lower the prominence threshold just slightly from  
362      0.1 to 0.09 we detect a third gap in both the OPAL and  
363      OPLIB datasets where one would be expected.

364      Previous modeling efforts (e.g. Feiden et al. 2021) have  
365      not identified multiple gaps. This is likely due to two  
366      reasons: (1), previous studies have allowed metallicity to  
367      vary across their model grids, further smearing the gaps  
368      out, and (2), previous studies have used more coarse  
369      underlying mass grids, obscuring features smaller than  
370      their mass step. While this dual-gap structure has not

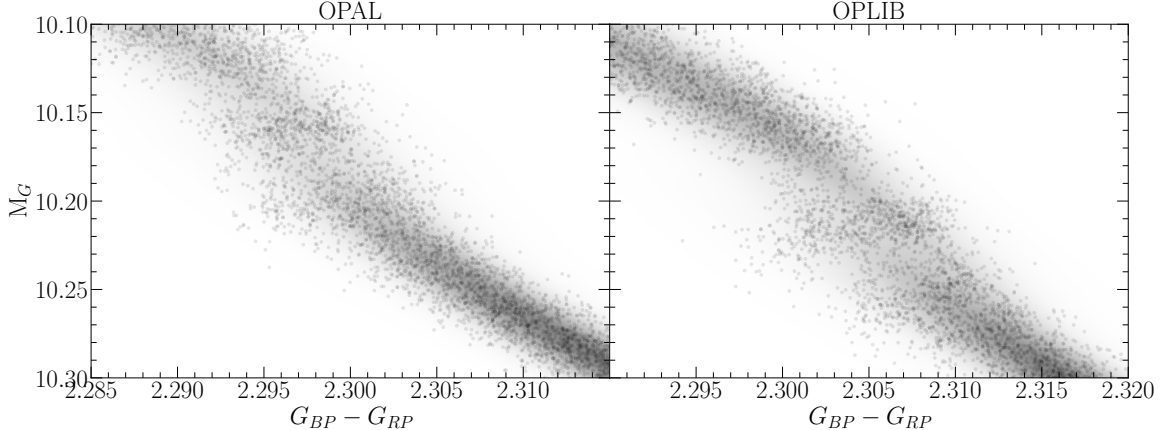


**Figure 7.** Population synthesis results for models evolved with OPAL (left) and models evolved with OPLIB (right). A Gaussian kernel-density estimate has been overlaid to better highlight the density variations.

been seen in models before, a more complex gap structure is not totally unprecedented as Jao & Feiden (2021) identifies an additional underdense region below the primary gap in EDR3 data. As part of a follow up series of papers, we are conducting further work to incorporate metallicity variations while still using the finer mass sampling presented here.

The mean gap location of the OPLIB population is at a fainter magnitude than the mean gap location of the OPAL population. Consequently, in the OPLIB sample the convective mixing events which drive the kissing instability begin happening at lower masses (i.e. the convective transition mass decreases). A lower mass range will naturally result in a fainter mean gap magnitude.

Mixing events at lower masses in OPLIB models are attributable to the radially thicker, at the same mass, radiative zones (Figure 9). This thicker radiative zone will take more time to break down at similar decay and is characteristic to OPLIB models as a result of their slightly lower opacities. A lower opacity fluid will have a more shallow radiative temperature gradient than a higher opacity fluid; however, as the adiabatic temperature gradient remains essentially unchanged as a function of radius, a larger interior radius of the model will remain unstable to radiation. This thicker radiative zone will increase the time it takes the core convective zone to meet up with convective envelope meaning that lower mass models can sustain a radiative zone for longer than they could otherwise; thus; lower opacities push the convective transition mass down. We can additionally see this longer lived radiative zone in the core  $^3\text{He}$  mass fraction, in which OPLIB models reach much higher concentrations — at approximately the same growth rate — for the same mass as OPAL models do (Figure 10).

The most precise published Gap location comes from Jao & Feiden (2020) who use EDR3 to locate the Gap at  $M_G \sim 10.3$ , we identify the Gap at a similar location in the GCNS data. **The Gap in populations evolved using OPLIB tables is closer to this measurement than it is in populations evolved using OPAL tables (Table 2).** It should be noted that the exact location of the observed Gap is poorly captured by a single value as the Gap visibly compresses across the width of the main-sequence, wider on the blue edge and narrower on the red edge such that the observed Gap has downward facing a wedge shape (Figure 1). This wedge shape is not successfully reproduced by either any current models or the modeling we perform here. We elect then to specify the Gap location where this wedge is at its narrowest, on the red edge of the main sequence.

The Gaps identified in our modeling have widths of approximately 0.03 magnitudes, while the shift from OPAL to OPLIB opacities is 0.05 magnitudes. With the prior that the Gaps clearly shift before noise is injected we know that this shift is real. However, the shift magnitude and Gap width are of approximately the same size in our synthetic populations. Moreover, Feiden et al. (2021) identify that the shift in the modeled Gap mass from  $[\text{Fe}/\text{H}] = 0$  to  $[\text{Fe}/\text{H}] = +0.5$  as  $0.04M_\odot$ , whereas we only see an approximate  $0.01 M_\odot$  shift between OPAL and OPLIB models. **Therefore, the Gap location will likely not provide a usable constraint on the opacity source.**

## 6. CONCLUSION

The Jao Gap provides an intriguing probe into the interior physics of M Dwarfs stars where traditional methods of studying interiors break down. However, before detailed physics may be inferred it is essential to have models which are well matched to observations. Here

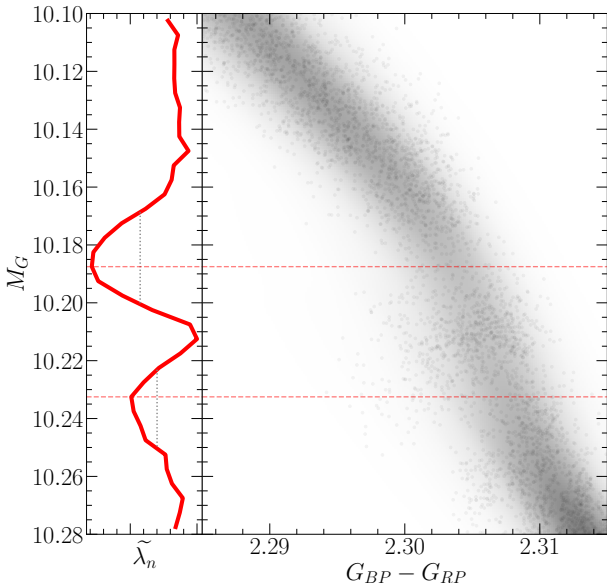
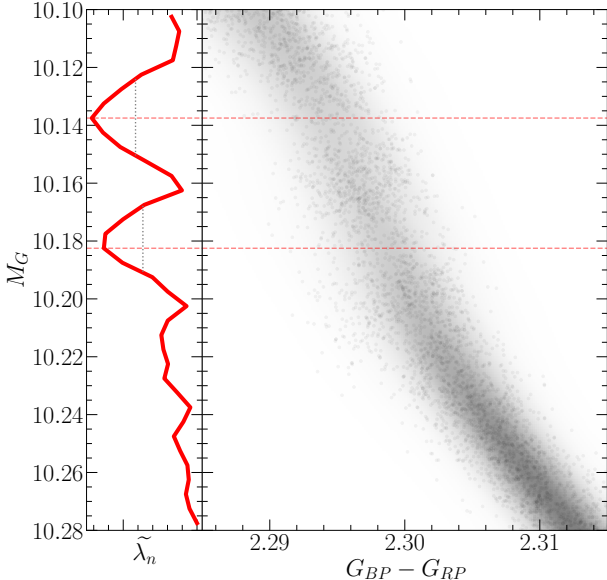


**Figure 8.** (right panels) OPAL (top) and OPLIB (bottom) synthetic populations. (left panels) Normalized linear number density along the magnitude axis. A dashed line has been extended from the peak through both panels to make clear where the identified Jao Gap location is wrt. to the population.

we investigate whether the OPLIB opacity tables reproduce the Jao Gap location and structure more accurately than the widely used OPAL opacity tables. We find that while the OPLIB tables do shift the Jao Gap location more in line with observations, by approximately 0.05 magnitudes, the shift is small enough that it is likely not distinguishable from noise due to population age and chemical variation. However, future measurement of [Fe/H] for stars within the gap will be helpful in con-

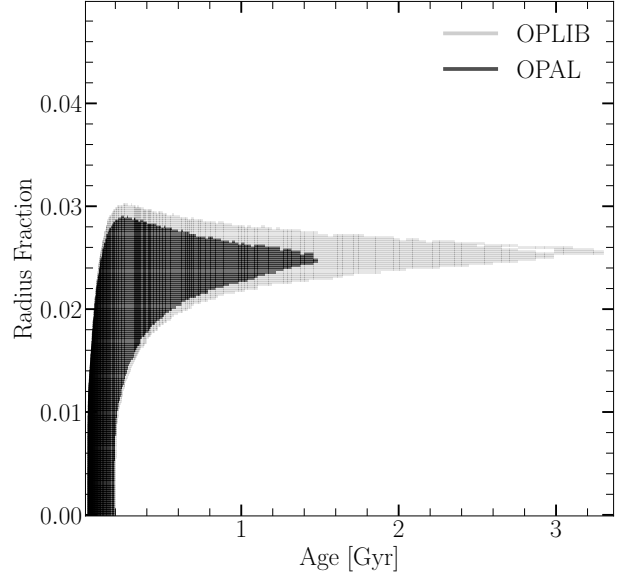


**Figure 9.** Portions of  $0.3526 M_{\odot}$  OPAL and OPLIB stellar models showing the interior shells which are radiative (black region). Note that for clarity only one convective mixing event from each model is shown. Note how the radiative zone in the OPLIB model is larger.

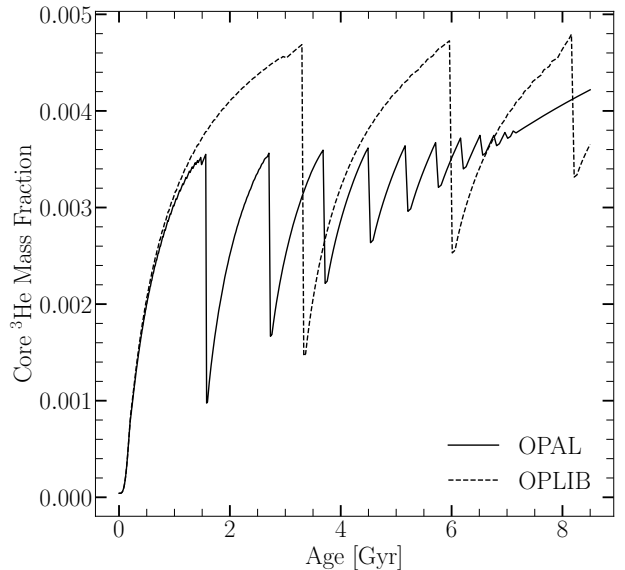


**Figure 10.** Core  ${}^3\text{He}$  mass fraction for  $0.3526 M_{\odot}$  models evolved with OPAL and OPLIB (within the Jao Gap's mass range for both). Note how the OPLIB model's core  ${}^3\text{He}$  mass fraction grows at approximately the same rate as the OPAL model's but continues uninterrupted for longer.

straining the degree to which the gap should be smeared by these theoretical models. Finally, we do not find that the OPLIB opacity tables help in reproducing the as yet unexplained wedge shape of the observed Gap.

454

## APPENDIX

455

## A. PYTOPSSCRAPE

456 pyTOPSScrape provides an easy to use command line and python interface for the OPLIB opacity tables accessed  
 457 through the TOPS web form. Extensive documentation of both the command line and programmatic interfaces is in  
 458 linked in the version controlled repository. However, here we provide a brief, illustrative, example of potential use.

459 Assuming pyTOPSScrape has been installed and given some working directory which contains a file describing a base  
 460 composition (“comp.dat”) and another file containing a list of rescalings of that base composition (“rescalings.dat”)  
 461 (both of these file formats are described in detail in the documentation), one can query OPLIB opacity tables and  
 462 convert them to a form mimicking that of type 1 OPAL high temperature opacity tables using the following shell  
 463 command.

464 \$ generateTOPStables comp.dat rescalings.dat -d ./TOPSCache -o out.opac -j 20

465 For further examples of pyTOPSScrape please visit the repository.

466

B. INTERPOLATING  $\rho \rightarrow R$ 

467 OPLIB parameterizes  $\kappa_R$  as a function of mass density, temperature in keV, and composition. Type 1 OPAL high  
 468 temperature opacity tables, which DSEP and many other stellar evolution programs use, instead parameterizes opacity  
 469 as a function of temperature in Kelvin,  $R$  (Equation B1), and composition. The conversion from temperature in keV  
 470 to Kelvin is trivial (Equation B2).

471  
472  
473

$$R = \frac{\rho}{T_6^3} \quad (\text{B1})$$

474  
475

$$T_K = T_{\text{keV}} * 11604525.0061657 \quad (\text{B2})$$

476 However, the conversion from mass density to  $R$  is more involved. Because  $R$  is coupled with both mass density and  
 477 temperature there is no way to directly convert tabulated values of opacity reported in the OPLIB tables to  
 478 their equivalents in  $R$  space. Instead we must rotate the tables, interpolating  $\kappa_R(\rho, T_{\text{eff}}) \rightarrow \kappa_R(R, T_{\text{eff}})$ .

479 To perform this rotation we use the `interp2d` function within `scipy`'s `interpolate` (Virtanen et al. 2020) module to  
 480 construct a cubic bivariate B-spline (Dierckx 1981) interpolating function  $s$ , with a smoothing factor of 0, representing  
 481 the surface  $\kappa_R(\rho, T_{\text{eff}})$ . For each  $R^i$  and  $T_{\text{eff}}^j$  reported in type 1 OPAL tables, we evaluate Equation B1 to find  
 482  $\rho^{ij} = \rho(T_{\text{eff}}^j, R^i)$ . Opacities in  $T_{\text{eff}}$ ,  $R$  space are then inferred as  $\kappa_R^{ij}(R^i, T_{\text{eff}}^j) = s(\rho^{ij}, T_{\text{eff}}^j)$ .

483 As first-order validation of this interpolation scheme we can perform a similar interpolation in the opposite direction,  
 484 rotating the tables back to  $\kappa_R(\rho, T_{\text{eff}})$  and then comparing the initial, “raw”, opacities to those which have gone  
 485 through the interpolations process. Figure 11 shows the fractional difference between the raw opacities and a set  
 486 which have gone through this double interpolation. The red line denotes  $\log(R) = -1.5$  where models will tend to sit  
 487 for much of their radius. Along the  $\log(R) = -1.5$  line the mean fractional difference is  $\langle \delta \rangle = 0.006$  with an uncertainty  
 488 of  $\sigma_{\langle \delta \rangle} = 0.009$ . One point of note is that, because the initial rotation into  $\log(R)$  space also reduces the domain of the  
 489 opacity function, interpolation-edge effects which we avoid initially by extending the domain past what type 1 OPAL  
 490 tables include cannot be avoided when interpolating back into  $\rho$  space.

491 This work has made use of the NASA astrophysical data system (ADS). We would like to thank Elisabeth Newton,  
 492 Aaron Dotter, and Gregory Feiden for their support and for useful discussion related to the topic of this paper.  
 493 Additionally, we would like to thank James Colgan and the Los Alamos T-1 group for their assistance with the OPLIB  
 494 opacity tables and support for the public release of pyTOPSScrape. We acknowledge the support of a NASA grant  
 495 (No. 80NSSC18K0634).

496 *Software:* The Dartmouth Stellar Evolution Program (DSEP) (Dotter et al. 2008), BeautifulSoup (Richardson  
 497 2007), mechanize (Chandra & Varanasi 2015), FreeEOS (Irwin 2012), pyTOPSScrape (Boudreux 2022)

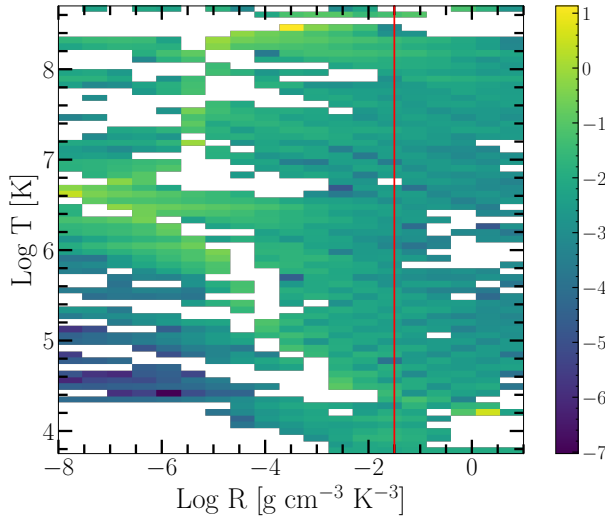


**Figure 11.** Log Fractional Difference between opacities in  $\kappa_R(\rho, T_{eff})$  space directly queried from the OPLIB web-form and those which have been interpolated into  $\log(R)$  space and back. Note that, due to the temperature grid of type 1 OPAL tables not aligning perfectly with the temperature grid OPLIB uses there may be edge effects where the interpolation is poorly constrained. The red line corresponds to  $\log(R) = -1.5$  where much of a stellar model's radius exists.

## REFERENCES

- 498 Amard, L., Palacios, A., Charbonnel, C., et al. 2019, A&A,  
499 631, A77, doi: [10.1051/0004-6361/201935160](https://doi.org/10.1051/0004-6361/201935160)
- 500 Bahcall, J. N., Serenelli, A. M., & Basu, S. 2005, ApJL,  
501 621, L85, doi: [10.1086/428929](https://doi.org/10.1086/428929)
- 502 Baraffe, I., & Chabrier, G. 2018, A&A, 619, A177,  
503 doi: [10.1051/0004-6361/201834062](https://doi.org/10.1051/0004-6361/201834062)
- 504 Boudreault, T. 2022, tboudreault/pytopsscraper:  
505 pyTOPSScraper v1.0, v1.0, Zenodo,  
506 doi: [10.5281/zenodo.7094198](https://doi.org/10.5281/zenodo.7094198).  
507 <https://doi.org/10.5281/zenodo.7094198>
- 508 Chabrier, G., & Baraffe, I. 1997, A&A, 327, 1039.  
509 <https://arxiv.org/abs/astro-ph/9704118>
- 510 Chandra, R. V., & Varanasi, B. S. 2015, Python requests  
511 essentials (Packt Publishing Ltd)
- 512 Choi, J., Dotter, A., Conroy, C., et al. 2016, ApJ, 823, 102,  
513 doi: [10.3847/0004-637X/823/2/102](https://doi.org/10.3847/0004-637X/823/2/102)
- 514 Colgan, J., Kilcrease, D. P., Magee, N. H., et al. 2016, in  
515 APS Meeting Abstracts, Vol. 2016, APS Division of  
516 Atomic, Molecular and Optical Physics Meeting  
517 Abstracts, D1.008
- 518 Creevey, O. L., Sordo, R., Pailler, F., et al. 2022, arXiv  
519 e-prints, arXiv:2206.05864.  
520 <https://arxiv.org/abs/2206.05864>
- 521 Dierckx, P. 1981, IMA Journal of Numerical Analysis, 1,  
522 267, doi: [10.1093/imanum/1.3.267](https://doi.org/10.1093/imanum/1.3.267)
- 523 Dotter, A., Chaboyer, B., Jevremović, D., et al. 2008, The  
524 Astrophysical Journal Supplement Series, 178, 89
- 525 Feiden, G. A., Skidmore, K., & Jao, W.-C. 2021, ApJ, 907,  
526 53, doi: [10.3847/1538-4357/abcc03](https://doi.org/10.3847/1538-4357/abcc03)
- 527 Ferguson, J. W., Alexander, D. R., Allard, F., et al. 2005,  
528 ApJ, 623, 585, doi: [10.1086/428642](https://doi.org/10.1086/428642)
- 529 Fontes, C. J., Zhang, H. L., Abdallah, J., J., et al. 2015,  
530 Journal of Physics B Atomic Molecular Physics, 48,  
531 144014, doi: [10.1088/0953-4075/48/14/144014](https://doi.org/10.1088/0953-4075/48/14/144014)
- 532 Gaia Collaboration, Smart, R. L., Sarro, L. M., et al. 2021,  
533 A&A, 649, A6, doi: [10.1051/0004-6361/202039498](https://doi.org/10.1051/0004-6361/202039498)
- 534 Hakel, P., Sherrill, M. E., Mazevet, S., et al. 2006, JQSRT,  
535 99, 265, doi: [10.1016/j.jqsrt.2005.04.007](https://doi.org/10.1016/j.jqsrt.2005.04.007)
- 536 Iglesias, C. A., & Rogers, F. J. 1996, ApJ, 464, 943,  
537 doi: [10.1086/177381](https://doi.org/10.1086/177381)
- 538 Irwin, A. W. 2012, FreeEOS: Equation of State for stellar  
539 interiors calculations, Astrophysics Source Code Library,  
540 record ascl:1211.002. <http://ascl.net/1211.002>
- 541 Jao, W.-C., & Feiden, G. A. 2020, AJ, 160, 102,  
542 doi: [10.3847/1538-3881/aba192](https://doi.org/10.3847/1538-3881/aba192)
- 543 —. 2021, Research Notes of the American Astronomical  
544 Society, 5, 124, doi: [10.3847/2515-5172/ac053a](https://doi.org/10.3847/2515-5172/ac053a)
- 545 Jao, W.-C., Henry, T. J., Gies, D. R., & Hambly, N. C.  
546 2018, ApJL, 861, L11, doi: [10.3847/2041-8213/aacd6](https://doi.org/10.3847/2041-8213/aacd6)
- 547 MacDonald, J., & Gizis, J. 2018, MNRAS, 480, 1711,  
548 doi: [10.1093/mnras/sty1888](https://doi.org/10.1093/mnras/sty1888)
- 549 Magee, N. H., Abdallah, J., Colgan, J., et al. 2004, in  
550 American Institute of Physics Conference Series, Vol.  
551 730, Atomic Processes in Plasmas: 14th APS Topical  
552 Conference on Atomic Processes in Plasmas, ed. J. S.  
553 Cohen, D. P. Kilcrease, & S. Mazavet, 168–179

- 554 Mansfield, S., & Kroupa, P. 2021, A&A, 650, A184,  
555 doi: [10.1051/0004-6361/202140536](https://doi.org/10.1051/0004-6361/202140536)
- 556 Nutzman, P., & Charbonneau, D. 2008, PASP, 120, 317,  
557 doi: [10.1086/533420](https://doi.org/10.1086/533420)
- 558 Richardson, L. 2007, April
- 559 Rodríguez-López, C. 2019, Frontiers in Astronomy and  
560 Space Sciences, 6, 76, doi: [10.3389/fspas.2019.00076](https://doi.org/10.3389/fspas.2019.00076)
- 561 Seaton, M. J., Yan, Y., Mihalas, D., & Pradhan, A. K.  
562 1994, MNRAS, 266, 805, doi: [10.1093/mnras/266.4.805](https://doi.org/10.1093/mnras/266.4.805)
- 563 Skrutskie, M. F., Cutri, R. M., Stiening, R., et al. 2006, AJ,  
564 131, 1163, doi: [10.1086/498708](https://doi.org/10.1086/498708)
- 565 Sollima, A. 2019, Monthly Notices of the Royal  
566 Astronomical Society, 489, 2377,  
567 doi: [10.1093/mnras/stz2093](https://doi.org/10.1093/mnras/stz2093)
- 568 van Saders, J. L., & Pinsonneault, M. H. 2012, ApJ, 751,  
569 98, doi: [10.1088/0004-637X/751/2/98](https://doi.org/10.1088/0004-637X/751/2/98)
- 570 Virtanen, P., Gommers, R., Oliphant, T. E., et al. 2020,  
571 Nature Methods, 17, 261, doi: [10.1038/s41592-019-0686-2](https://doi.org/10.1038/s41592-019-0686-2)